

# Bright single photon emitters with enhanced quantum efficiency in a two-dimensional semiconductor coupled with dielectric nano-antennas

Luca Sortino,<sup>1,2,\*</sup> Panaiot G. Zotev,<sup>1</sup> Catherine L. Phillips,<sup>1</sup> Alistair J. Brash,<sup>1</sup> Javier Cambiasso,<sup>3</sup> Elena Marensi,<sup>4</sup> A. Mark Fox,<sup>1</sup> Stefan A. Maier,<sup>2,3</sup> Riccardo Sapienza,<sup>3</sup> and Alexander I. Tartakovskii<sup>1,†</sup>

<sup>1</sup>*Department of Physics and Astronomy, University of Sheffield, Sheffield, S3 7RH, United Kingdom*

<sup>2</sup>*Chair in Hybrid Nanosystems, Nanoinstitute München, Faculty of Physics, Ludwig-Maximilians-Universität München, 80539 München, Germany*

<sup>3</sup>*The Blackett Laboratory, Department of Physics, Imperial College London, London, SW7 2BW, United Kingdom*

<sup>4</sup>*IST Austria, Am Campus 1, 3400 Klosterneuburg, Austria*

(Dated: March 1, 2025)

Single photon emitters (SPEs) in two-dimensional (2D) atomically-thin semiconductor WSe<sub>2</sub> [1–5] can be deterministically positioned using localized strain induced by underlying nano-structures [6, 7], potentially opening a route for SPE integration with nano-photonic structures and devices. Here, we couple SPEs in monolayer WSe<sub>2</sub> to broadband optical cavities formed by high-refractive-index gallium phosphide (GaP) dielectric nano-antennas [8, 9] also providing the monolayer deformation [10] required for creating the SPEs. We find that in comparison with WSe<sub>2</sub> SPEs formed on non-resonant SiO<sub>2</sub> pillars, SPEs on resonant GaP nano-antennas show 10<sup>2</sup> to 10<sup>4</sup> times brighter photoluminescence (PL) accompanied by low PL saturation pulse energy densities < 30 nJ/cm<sup>2</sup> and PL lifetimes from 2 to 200 ns. We show that the key to these observations is the increased quantum efficiency (QE) in SPEs on the GaP nano-antennas, reaching 86%, with an average of 21% compared to 4% in SPEs on SiO<sub>2</sub>. The bright PL and high QE enables us to explore the SPE PL dynamics at ultra-low laser powers. From the power-dependent PL rise times, we reveal the ns-scale lifetimes of dark exciton reservoir in the 2D WSe<sub>2</sub> feeding the SPEs, as well as its population decay due to Auger processes at higher powers, providing insight into the PL saturation phenomenon in WSe<sub>2</sub> SPEs. We further measure the coherence time of a high QE SPE, and show that its PL linewidth is limited by intrinsic dephasing processes. Our work establishes dielectric nano-antennas as a platform for high-efficiency quantum emission in 2D SPEs.

SPEs in 2D semiconducting WSe<sub>2</sub> open attractive perspectives for few-atom-thick devices in quantum technologies owing to favourable excitonic properties [11] and the integration with arbitrary substrates, including nano-structured surfaces [9, 10]. Several theoretical models have been proposed to provide insight into the origin of

SPEs observed in the cryogenic PL spectra of 2D WSe<sub>2</sub> [12–15]. Their occurrence was explained by the presence of strain-induced potential traps for excitons [13], momentum-dark states [12] or various types of defects [14, 15]. While the exact origin is still under debate, first significant steps have been made to integrate WSe<sub>2</sub> SPEs in devices, including electroluminescent structures [16–18], waveguides [19, 20] and tunable high-Q microcavities [21]. Moreover, the evidence of a biexciton cascade emission [22] and hole spin initialization [23] exemplifies the possibility for more advanced development of quantum light sources based on 2D-WSe<sub>2</sub>. An appealing approach for the scalable and controllable fabrication of SPEs in WSe<sub>2</sub> is the use of strain engineering for their deterministic positioning. Based on this idea, SiO<sub>2</sub> [7] or polymer nano-pillars [6] have been employed to induce arrays of SPEs in atomically thin WSe<sub>2</sub>. In a similar approach, nano-structures made of noble metals were also employed where, due to the enhancement of the near-field intensity by plasmonic resonances, increased spontaneous emission rates were demonstrated [24]. However, plasmonic nano-antennas are known for large non-radiative losses and, to prevent the quenching of SPEs PL, WSe<sub>2</sub> layers were separated by a few nm thick dielectric spacer from the metallic surface, increasing the fabrication complexity and reducing the near-field coupling efficiency [24]. In contrast, the high-refractive-index dielectric materials used in our work offer a lossless alternative to metals [25]. Sub-wavelength dielectric nano-antennas exhibit optical Mie resonances carrying both electric and magnetic responses [26]. High-index dielectric nano-antennas have also been recently shown to provide an efficient approach for the enhancement of light-matter interaction, as well as improved emitted light directionality, in molecules [8], colloidal quantum dots [27] and excitons in 2D semiconductors [9, 28].

Here, we show that bright SPEs with enhanced QE can be induced in WSe<sub>2</sub> monolayers transferred on top of GaP dielectric nano-antennas. As a reference, we compare, both experimentally and by numerical simulation, the SPEs coupled to the high-index GaP nano-antennas with SPEs in WSe<sub>2</sub> transferred on low-index SiO<sub>2</sub> nano-

pillars. In the WSe<sub>2</sub> placed on top of the GaP nano-antennas, the SPEs form in close proximity to the maxima of the electromagnetic fields confined at the nano-antennas surface. For such SPEs, we predict from numerical simulations PL enhancement factors,  $\langle EF \rangle$  [9, 29], up to 800, compared with the SPEs coupled to SiO<sub>2</sub>. Experimentally, we observe an even larger PL enhancement of up to  $10^4$  which we explain by a very large enhancement of the QE, defined as the probability to detect a photon per excitation pulse, in SPEs on GaP nano-antennas. We observe high QE SPEs exhibiting a wide range of PL lifetimes from 2 up to 200 ns, indicating that radiative lifetime of SPEs in WSe<sub>2</sub> could be much longer than commonly reported values of  $\leq 10$  ns. We estimate the values of QE by accounting for all elements of the experimental set-up, and find QE exceeding 80% and reaching  $21 \pm 3\%$  on average for SPEs on GaP nano-antennas compared with  $4 \pm 2\%$  average for SPEs on SiO<sub>2</sub> nano-pillars. Owing to the high QE values, we investigate a previously inaccessible regime of PL dynamics in SPEs providing important insight for mechanisms responsible for populating SPEs and eventually leading to their PL saturation at high powers, which, as we find, is strongly influenced by the decay of the dark exciton population via non-radiative exciton-exciton annihilation. Despite the improved QE, the SPE coherence time, that we also measure in this work, remains low, of the order of a few ps for the off- and quasi-resonant excitation that we employed. Our results highlight that high-refractive-index nano-antennas, exhibiting near-field optical enhancement, provide strong advantages for producing bright SPEs in WSe<sub>2</sub> monolayers. We also shed light on the limitations of low-refractive-index SiO<sub>2</sub> and polymer nano-pillars. WSe<sub>2</sub> SPEs positioned on such structures require relatively high pumping powers for their operation, resulting in further increase in non-radiative decay due to exciton-exciton annihilation, and thus reduced brightness of non-classical light emission.

### Positioning WSe<sub>2</sub> SPEs on GaP nano-antennas

We use GaP nano-antennas composed of two closely spaced nano-pillars (Fig.1a), referred to as ‘dimer’ below (see also Supplementary Fig.1a). They exhibit an enhancement of the electromagnetic near-field intensity, as a result of the high refractive index ( $n_{\text{GaP}} \approx 3.2$ ) and the hybridization of the optical resonances of each individual pillars (see Supplementary Notes I & II). This is demonstrated in Fig.1a, where we show the calculated electric field intensity of the scattered radiation,  $|E|^2$ , normalized by the intensity  $|E_0|^2$  of the normally incident plane wave with linear polarization along the axis connecting the centres of the nano-pillars. The profile in Fig.1a corresponds to the top surface of the GaP dimer ( $z = 200$  nm) having individual pillar radii of 150 nm. The enhancement of  $|E|^2$  compared with  $|E_0|^2$  exceeds 10 times and is particularly pronounced in the gap between the pillars [8, 9, 30]. As shown in Fig.1b, under the

same excitation conditions, a SiO<sub>2</sub> nano-pillar ( $r = 150$  nm,  $h = 100$  nm) does not show strong electromagnetic resonances, as a consequence of its low refractive index ( $n_{\text{SiO}_2} \approx 1.5$ ).

A dipole emitter, such as an exciton in an SPE, spectrally and spatially overlapping with the near-field of the antenna, is expected to exhibit an enhanced light emission intensity [29]. This is a result of the product of the three main factors giving rise to the PL enhancement factor  $\langle EF \rangle$  [9, 29]. Depending on the relative position and orientation of its dipole moment, the emitter experiences an increased local density of states and thus an enhanced spontaneous emission rate [31] via the Purcell effect, introducing a factor  $F_p$ , directly improving the overall quantum efficiency,  $\text{QE} = F_p \gamma_{\text{rad}} / (F_p \gamma_{\text{rad}} + \gamma_{\text{nr}})$ , where  $\gamma_{\text{rad}}$  and  $\gamma_{\text{nr}}$  are the rates of the radiative and non-radiative decay, respectively. In the absence of the Purcell effect  $F_p=1$  and we assumed  $\gamma_{\text{rad}} \ll \gamma_{\text{nr}}$ . The antenna also modifies the dipole far field emission pattern, leading to an increased light collection efficiency above the antenna ( $\eta_{\text{obj}}$ ) within the given numerical aperture (NA) of the objective lens used in the detection system. Finally, the enhanced absorption of light in the material coupled to the antenna (in our case, a monolayer WSe<sub>2</sub>), quantified by the excitation rate proportional to the intensity of the local near-field,  $\gamma_{\text{exc}} \propto (|E|/|E_0|)^2$  (Fig.1a-b), should in principle lead to a more efficient excitation of an SPE. As shown in Fig.1c-e, we carried out numerical simulations (see Methods and Supplementary Note II) to extract the values of these three parameters for a dipole emitting at  $\lambda_{\text{em}} = 750$  nm coupled to either GaP dimer nano-antennas (data in red) or to SiO<sub>2</sub> nano-pillars (blue). The dipole is placed at the positions where the interaction is maximized [9] and is aligned perpendicularly to the edge of the nano-pillar (Supplementary Fig.3a). As shown in Fig.1c-d, a GaP nano-antenna may induce an enhancement of the PL intensity by at least two orders of magnitude [8, 9, 30], compared to SiO<sub>2</sub> nano-pillars, as a consequence of the increase in both the spontaneous emission rate  $F_p$  (Fig.1c), the excitation rate  $\gamma_{\text{exc}}$  (Fig.1d), and a relatively modest effect in the collection efficiency  $\eta_{\text{obj}}$  (Fig.1e), as expected from the similar geometries of dimers and single pillars.

In order to experimentally examine these effects, we transferred WSe<sub>2</sub> monolayers on top of an array of GaP nano-antennas (see Methods and Supplementary Note III) and on SiO<sub>2</sub> nano-pillars as a reference (see Supplementary Note IV). With this approach, we achieve localized strain in the monolayer, introduced by the underlying nano-structure [10], which promotes the occurrence of localized SPEs at cryogenic temperatures [6, 7]. The samples are placed in a gas exchange cryostat, at a temperature of  $T = 4$  K, and excited (unless stated otherwise) with a non-resonant pulsed laser at 638 nm with 90 ps pulse width and a variable repetition rate. The laser excites below the GaP bandgap and is absorbed only by

the WSe<sub>2</sub> monolayer. The inset in Fig.1f shows a map of the integrated PL intensity from a WSe<sub>2</sub> monolayer deposited on top of a GaP dimer nano-antenna ( $r = 250$  nm). The PL signal exhibits a strong localization at the nano-antenna position, with negligible emission from the surrounding area where PL from the unstrained WSe<sub>2</sub> monolayer is expected. As shown in Fig.1f, we observe bright and narrow PL lines, with suppressed background PL from the band of localized states in WSe<sub>2</sub> as usually observed when WSe<sub>2</sub> is deposited on SiO<sub>2</sub> pillars (Supplementary Fig.7a). We demonstrate the single-photon operation of the localized emitters in photon correlation measurements (see Methods). Fig.1g shows the second order correlation function,  $g^{(2)}(\tau)$ , for the emitter shown in Fig.1f, excited at  $\lambda_{\text{exc}} = 725$  nm, approximately 35 meV below the WSe<sub>2</sub> A-exciton resonance. The pronounced anti-bunching behavior at zero time delay exhibits  $g^{(2)}(0) = 0.26 \pm 0.03$ , confirming the non-classical photon emission statistics. In Supplementary Note V, we further correlate the SPEs emission energy to the strain induced in the 2D layer by the nano-antennas. Stretching of the WSe<sub>2</sub> monolayer results in a progressively larger red-shift of the SPE emission when deposited on nano-antennas with smaller radii [10]. This behavior, analogous to the red-shift of WSe<sub>2</sub> excitons under tensile deformation [10], confirms the impact of strain on the confinement potential and emission energy of WSe<sub>2</sub> SPEs.

**Quantum efficiency enhancement of SPEs on GaP nano-antennas** We analysed more than 50 SPEs on GaP dimer nano-antennas, with radii ranging from 150 nm up to 300 nm, selecting localized WSe<sub>2</sub> emitters with sub-meV linewidths. For these emitters we observed common features such as linearly polarized emission, saturation of the PL intensity under increase excitation power, as well as PL lifetimes in the ns range (see also Supplementary Note III). Fig.2a shows the values of the PL intensity for SPEs on GaP nano-antennas (red dots) and on SiO<sub>2</sub> nano-pillars (blue dots), acquired in the PL saturation regime and normalized to the average excitation pump power. The plot also shows the PL peak position for each studied SPE, where no correlation between the intensity and spectral position is observed. For SPEs coupled to GaP nano-antennas, we observe from two to four orders of magnitude higher power-normalized PL intensity, compared to SPEs found on SiO<sub>2</sub> nano-pillars. Further insight into this behavior is provided by the SPE PL saturation powers, presented in Fig.2b. Since we used different repetition rates from 5 to 80 MHz in these measurements due to a large variation in the PL lifetimes, in Fig.2b we plot the energy per pulse value  $P_{\text{sat}}$ , defined as the time-integrated average power divided by the laser repetition rate. We readily observe more than three orders of magnitude lower saturation pulse energies for the emitters on GaP nano-antennas. In our case, 1 fJ pulse energy corresponds to the energy density per pulse of 30 nJ/cm<sup>2</sup>. Nonetheless, for such low powers, the SPEs

coupled to GaP nano-antennas provide some of the highest counts per second ( $>30,000$ ) so far observed in TMD monolayers. In what follows, we will consider the factors that could contribute to this observation.

One of the obvious factors, expected to contribute to the reduced values of  $P_{\text{sat}}$  is the enhanced absorption rate ( $\gamma_{\text{exc}}$ ) in WSe<sub>2</sub> monolayers coupled to GaP nano-antennas. However, this can only account for a reduction of the saturation power of up to 40 times as predicted by our simulations (Fig.1d). A similar maximum enhancement for the power-normalized PL intensity may be expected due to the enhanced  $\gamma_{\text{exc}}$ . Thus, additional factors need to be considered, mostly linked to the exciton dynamics and QE of the combined 2D-WSe<sub>2</sub>/SPE system. In Fig.2c we compare PL lifetimes of SPEs on GaP and on SiO<sub>2</sub>. For the SPEs on the SiO<sub>2</sub> nano-pillars we observe lifetimes on the order of 10 ns, consistent with previous reports [6, 7]. On the contrary, the SPEs on the GaP nano-antennas exhibit a broad distribution of lifetime values, ranging from 2 ns up to more than 200 ns. While the radiative lifetimes of SPEs in WSe<sub>2</sub> are dependent on the shape and confinement energy of the strain potential, the PL decay dynamics is defined by the relationship between the radiative and non-radiative rates: if one of the rates is much shorter than the other, it will define the PL decay time. In order to shed light on the relationship between these rates, in Fig.2d we plot the SPEs fluorescence lifetime intensity distribution (FLID)[33]. The SPEs on SiO<sub>2</sub> exhibit low PL emission with relatively short lifetimes (blue area). In SPEs coupled to GaP nano-antennas we observe either a much higher PL intensity and similar lifetimes, or longer lifetimes with comparable brightness (red area in Fig.2d). The QE of an SPE under pulsed excitation can be estimated from the number of detected photons at saturation, divided by the laser repetition rate [24]. After taking into account the losses of the experimental set-up and the collection efficiency of the nano-antenna from numerical simulations (Supplementary Note VI), we estimate an average QE for SPEs coupled to GaP nano-antennas of  $21 \pm 3\%$ , with a maximum value reaching 86% corresponding to an effective single photon generation rate of 69 MHz at 80 MHz laser excitation rate. For SPEs on SiO<sub>2</sub> nano-pillars we estimate an average QE of  $4 \pm 2\%$  consistent with previous reports [24].

We thus conclude that the PL decay times of SPEs on SiO<sub>2</sub> nano-pillars are mainly defined by non-radiative processes, and that the true radiative lifetimes should by far exceed the measured decay times of  $\approx 10$  ns. On the other hand, for the SPEs on GaP nano-antennas exhibiting high QE, the lifetimes are mostly defined by the radiative decay, which, as we can conclude from Fig.2d, vary between 2 and 200 ns. Comparing this with the SPEs on SiO<sub>2</sub>, we can conclude that the high QE SPEs on GaP exhibiting lifetimes of the order of 10 ns or shorter are most likely affected by the Purcell enhancement in-

creasing their radiative rates, possibly positioned in the near-field hot spots. The high QE SPEs with PL decay times  $>10$  ns clearly must experience much slower non-radiative processes than SPEs on  $\text{SiO}_2$ , as the non-radiative lifetimes must be slower than the measured PL decay times. SPEs with PL lifetimes in the range of 100 ns were previously observed only in monolayer  $\text{WSe}_2$  encapsulated in hexagonal boron nitride [15], known for suppressing the non-radiative processes. In our case, possible causes could be the intrinsic long radiative lifetime of  $\text{WSe}_2$  SPEs, high surface quality of crystalline GaP structures, or that some SPEs are formed in the suspended part of the monolayer in proximity to the near-field hotspot and between the pillars [10]. We cannot exclude that some of the SPEs with PL decay times  $>10$  ns still experience Purcell enhancement, as the observed variation of the PL decay times exceeds one order of magnitude.

**Dynamics of exciton formation in strain-induced SPEs** SPEs in  $\text{WSe}_2$  are attributed to the occurrence of strain-induced local potential minima [6, 34], essentially zero-dimensional (0D), that can host a small number of confined excitons, similar for example to semiconductor quantum dots [35]. Contrary to other group-VI TMDs, tensile strain in  $\text{WSe}_2$  results in the lowering of the conduction band (CB) minimum and the rise of the valence band (VB) maximum, as shown in Fig.3a, both located at the K points in the momentum space [10, 36]. This creates an energy landscape where a very small fraction of the 2D exciton population may be captured into such 0D centres, giving rise to non-classical light emission from confined states, at photon energies lower than that of both bright and dark excitons in unstrained  $\text{WSe}_2$ .

As shown in Fig.2, in the case of  $\text{WSe}_2$  placed on GaP nano-antennas, both the quantum yield and brightness of the SPEs are greatly enhanced, allowing new insight into the exciton dynamics in this hybrid 2D-0D system. Fig.3b shows a PL spectrum for a SPE exhibiting QE of  $86 \pm 3\%$ . Fig.3c shows the time-resolved PL decay for the same SPE measured with 20 MHz repetition rate. The PL decay curves are obtained at different powers of 1, 100 and 1000 nW considerably below, close and considerably above the saturation power, respectively. For clarity, the inset zooms in on the short times after the laser pulse excitation. At low power we clearly observe a ns-scale rise time, which shortens as the power is increased also accompanied by a relatively weak shortening of the PL decay time.

We fit the data with a simple empirical model assuming an exciton reservoir, which feeds excitons into the SPE, as shown in Fig.3d. The model can be solved analytically (see Supplementary Note VII for more details) and is used to fit the data, as shown in the inset of Fig.3c, providing rise and decay times plotted in Fig.3e-f. Here, we see that as the power is increased the rise time,  $\tau_{\text{rise}}$ , changes strongly from 1.7 ns to times approaching the ex-

perimental resolution, whereas the PL decay time  $\tau_{\text{decay}}$  decreases from 8.5 to 7.4 ns.

In order to understand this behavior, we consider several processes, which influence both the populations of the high energy 2D exciton reservoir and the SPE itself. We argue that the exciton reservoir with the population  $n_X$  in Fig.3d corresponds to the population of dark excitons, which we infer from the very slow PL rise time of 1.7 ns at low power, in contrast to the expected lifetime of the bright excitons of a few ps [37, 38]. The dark excitons decay mostly via sample-specific non-radiative recombination with a rate  $\Gamma_{\text{nr}}^X$  and, importantly, via the exciton-exciton (Auger) annihilation [39, 40], which grows with the increasing power as  $\Gamma_A n_X^2$ . Trapping of dark excitons with a rate  $\Gamma_{\text{trap}}$  into the strain-induced SPE is responsible for a negligible reduction of  $n_X$ , as the anti-bunching photon emission implies that only one exciton per laser excitation cycle can be created in the SPE. We thus also introduce a probability  $n_1$  for the SPE to be filled with an exciton with  $0 \leq n_1 \leq 1$ . The trapping of the dark excitons is the only source of the SPE population, and is included as a term  $\Gamma_{\text{trap}}(1 - n_1)n_X$  in the equations below. Here we take into account the effect of the SPE occupancy on the reduced efficiency of the exciton trapping with the factor  $(1 - n_1)$ , providing one of the mechanisms for the PL saturation with increasing power observed in the experiment. The population of the SPE decays radiatively and non-radiatively with rates  $\Gamma_r$  and  $\Gamma_{\text{nr}}$ , respectively. Here, for simplicity we neglect the SPE's internal confined state structure, which we uncover in PL excitation experiments (see Fig.4 for details). The rate equations capturing the behavior of the three-level system depicted in Fig.3d are shown below:

$$\frac{dn_X}{dt} = -[\Gamma_{\text{nr}}^X + \Gamma_{\text{trap}}(1 - n_1)]n_X - \Gamma_A n_X^2 \quad (1)$$

$$\frac{dn_1}{dt} = -(\Gamma_r + \Gamma_{\text{nr}})n_1 + \Gamma_{\text{trap}}(1 - n_1)n_X \quad (2)$$

We estimate that for 1 nW laser power at 20 MHz repetition rate and 5% light absorption in  $\text{WSe}_2$ , the dark exciton density  $n_X \approx 3 \cdot 10^8 \text{ cm}^{-2}$  will be created. This is probably the lower bound, as the near-field electric field enhancement can locally lead to the increase of this value by a factor exceeding 10. At this low power limit, Auger annihilation can be neglected [39] and the unsaturated SPE emission leads to an average (per pulse)  $n_1 \ll 1$ . The PL rise dynamics is then defined by the predominately non-radiative decay of the dark excitons reservoir ( $\Gamma_{\text{nr}}^X$ ). As the power is increased, and both  $n_X$  and  $n_1$  grow, two additional processes become important: the Auger annihilation described by the term  $\Gamma_A n_X^2$  and the saturation of the SPE with the corresponding term  $\Gamma_{\text{trap}}(1 - n_1)n_X$ . For the powers presented in Fig.3,  $n_X(t=0)$  is estimated to be of the order of  $10^{10} \text{ cm}^{-2}$  for the power of 100 nW and  $10^{11} \text{ cm}^{-2}$  for 1000 nW, in

the range where the Auger annihilation was found to be very efficient [39, 40].

While a more detailed study at low powers could help to separate the contributions from Auger annihilation and SPE saturation, it is possible that in the high power regime the SPE PL saturation occurs not because of the state-filling effect, but due to the very fast non-radiative depletion of the dark exciton reservoir. In case of the bright and high QE SPEs in WSe<sub>2</sub>/GaP nano-antenna system, high photon counts can be achieved at relatively low excitation powers, thus circumventing the requirement for increased pumping. On the other hand, in the SPEs in WSe<sub>2</sub> on SiO<sub>2</sub> nano-pillars, where the both QE and brightness are low, increased pumping is required to observe the SPE PL. This has a negative effect on the population of the reservoir via Auger annihilation and thus, through such negative feedback, leads to the requirement to further increase the power. Eventually, both the low QE and its reduction due to the Auger annihilation lead to a very large three order of magnitude increase in the saturation powers in the SPEs in WSe<sub>2</sub> on SiO<sub>2</sub> nano-pillars compared with those on GaP nano-antennas, as seen in Fig.2.

**Coherence of a strain-induced SPE** The coherence of WSe<sub>2</sub> SPEs has been previously investigated only under high power densities and non-resonant excitation [24]. Here, we evaluated the first-order correlation function,  $g^{(1)}(\tau)$ , for the SPE shown in Fig.4a, in a Mach-Zender interferometer set-up [41] and compared different excitation schemes (see Methods). We employed an above-band excitation using a 1.96 eV (638 nm) cw laser, corresponding to an energy higher than the A-exciton resonance in monolayer WSe<sub>2</sub> (dashed line in Fig.4a). Under these conditions, high energy excitons are created in the continuum of states above the excitonic resonance, introducing dephasing for instance via scattering with phonons and impurities or via exciton-exciton interactions. To reduce the impact of such processes, we also used a quasi-resonant excitation with a cw laser at 1.71 eV (725 nm). As shown in Fig.4a, this excitation is resonant with higher energy states within the SPE [1]. Fig.4b shows the measured fringe contrast,  $\nu(\tau)$ , of the WSe<sub>2</sub> SPE under the two excitation schemes (see Methods). By fitting the observed decay of the fringe contrast with a single exponential decay function,  $g^{(1)}(\tau) \approx \exp(-|\tau|/T_2)$ , we extract a coherence time of  $T_2 = 3.12 \pm 0.40$  ps under quasi resonant excitation, and of  $T_2 = 2.83 \pm 0.20$  ps for above band excitation. The differences between the excitation schemes have a negligible effect on the SPE coherence, implying a complex relaxation processes within the confined states of the SPE. We find that the PL full-width at half maximum (FWHM) of  $\approx 450$   $\mu$ eV corresponds to the observed value of  $T_2 = 2.9$  ps (FWHM =  $2\Gamma = 2\hbar/T_2$ ), indicating that the coherence of the studied SPE is limited by pure dephasing, which we attribute to interactions with phonons during the exciton relaxation [42], as

for the excitation power  $< 20$  nW used in the experiment the contribution of Auger annihilation can be excluded. The observed SPEs  $T_2$  values are one order of magnitude higher than those reported for monolayer WSe<sub>2</sub> of 0.3 ps [42]. Interferometric measurements in resonance with the SPE optical transition could be employed to gain access to the intrinsic coherence times of strain-induced SPEs.

**Conclusions** In summary, we have demonstrated that high-refractive-index GaP nano-antennas offer an efficient approach for nano-scale positioning and QE enhancement in strain-induced SPEs in monolayer WSe<sub>2</sub>. We report the brightest non-classical light emission in 2D TMD semiconductors, excited with energy densities per laser pulse below 30 nJ/cm<sup>2</sup>, more than one order of magnitude larger than those reported for WSe<sub>2</sub> SPEs on plasmonic nano-structures [24] where large Purcell enhancements were observed. We found  $10^2$  to  $10^4$  enhancement of the PL intensity comparing WSe<sub>2</sub> SPEs coupled to GaP nano-antennas with those placed on low-refractive-index SiO<sub>2</sub> nano-pillars. We demonstrate that this is primarily caused by the greatly increased QE in the 2D/0D WSe<sub>2</sub> system coupled to GaP nano-antennas. This allows SPE operation at low exciton densities, thus avoiding exciton-exciton annihilation, which, as our time-integrated and time-resolved PL experiments imply, have a dramatic impact on the efficiency of SPEs on SiO<sub>2</sub> nano-pillars. We further shed light on the radiative time of WSe<sub>2</sub> emitters, observing a large number of SPEs with a high QE, due to the Purcell enhancement, and at the same time exhibiting a broad range of lifetimes from 2 to 200 ns. Our work suggests that hybrid systems composed of 2D semiconductors coupled to dielectric nano-antennas are a powerful means for control over light emission on the nanoscale, particularly where deterministic control over defect placement can be achieved [43].

## Methods

**Sample fabrication** The GaP dimer nano-antennas were fabricated using electron beam lithography, followed by several wet and dry etching steps as described in Ref.[8]. Arrays of nano-antennas separated by 4  $\mu$ m were made. The dimers had a gap of  $\approx 50$  nm, a height of 200 nm and nano-pillar radii ( $r$ ) of 150, 200, 250 and 300 nm. Atomically thin monolayers of WSe<sub>2</sub> were mechanically exfoliated from commercially available bulk single crystals (HQ Graphene) onto polydimethylsiloxane (PDMS) polymer substrates. The monolayer thickness was identified by examining room temperature PL with an imaging method described in Ref.[44]. The monolayers were then transferred on top of the GaP nano-antenna array, by using the same PDMS substrates, with an all-dry transfer technique in a home-built transfer setup [45].

**Optical spectroscopy** Low temperature PL spectroscopy was carried out with a sample placed in low pressure He exchange gas within a confocal microscope

platform allowing free space optical access and high precision sample positioning (Attocube). The whole microscope stick was inserted in a liquid helium transport dewar (Cryo Anlagenbau GmbH) and a nominal sample temperature of 4 K was used in all reported experiments. The excitation from the lasers used in this work was delivered through single-mode fibres to the optical breadboard placed at the top of the microscope stick, where it was collimated and directed onto the sample through a window at the top of the stick. For pulsed excitation we used a diode laser (PicoQuant) at 638 nm, with a variable repetition rate from 5 to 80 MHz and a pulse width of 90 ps. For continuous wave excitation, we used a tunable Ti-Sapphire laser (M Squared SOL-STIS). PL emitted by the sample was collected with an aspheric lens ( $NA = 0.64$ ) and coupled at the breadboard into a single-mode optical fibre, which delivered it to a spectrometer (Princeton Instruments SP2750), where it was detected with a high-sensitivity liquid nitrogen cooled charge-coupled device (Princeton Instruments PyLoN). For the time-resolved spectroscopy, the PL was also sent through the spectrometer to another exit port, where it was measured with an avalanche photodiode (ID100-MMF50) connected to a photon counting card (Becker and Hickl SP-130). A Hanbury-Brown-Twiss set-up used for the evaluation of the background-corrected[32] second-order correlation function ( $g^{(2)}(\tau)$ ) was equipped with two superconducting nanowire single photon detectors (Single Quantum) and a similar photon counting card.

**Coherence measurements** For evaluation of the first-order correlation function ( $g^{(1)}(\tau)$ ), we used a Mach-Zender interferometer set-up [41] with a phase shifter in one arm and a variable optical delay in the other. By sweeping the voltage of the phase shifter, the interference of light emitted by the SPE was measured using an avalanche photodiode at one output port of the interferometer. By measuring the intensity at the local maxima ( $I_{\max}$ ) and minima ( $I_{\min}$ ) of the interference fringes, we evaluate the fringe contrast ( $\nu$ ) as:

$$\nu = \frac{I_{\max} - I_{\min}}{I_{\max} + I_{\min}} \quad (3)$$

This procedure was repeated for increasing delay times, until the fringes were no longer resolved. The relationship between the fringe contrast and the first-order correlation function is given by the following equation:

$$\nu(\tau) = (1 - \epsilon) \frac{|g^{(1)}(\tau)|}{g^{(1)}(0)} \quad (4)$$

where  $1 - \epsilon$  is the maximum resolvable fringe contrast in the set-up and  $|g^{(1)}(\tau)|$  is the first order correlation function excluding the fast oscillations at the emitter frequency. [41]. In the absence of any spectral diffusion, the fringe contrast as a function of time follows a single

exponential decay, with an exponential fit allowing the evaluation of the coherence time ( $T_2$ ) of the emitter.

**Simulations** The distributions of the electric field in Fig.1 were calculated with a commercial finite-difference time-domain software (Lumerical Inc.). In the simulations we illuminated the structure with a linearly polarized plane wave at  $\lambda = 750$  nm with a normal incidence from the vacuum side of the substrate. See Supplementary Note II for further details on the simulations.

---

\* luca.sortino@physik.uni-muenchen.de

† a.tartakovskii@sheffield.ac.uk

- [1] P. Tonndorf, R. Schmidt, R. Schneider, J. Kern, M. Buscema, G. a. Steele, A. Castellanos-Gomez, H. S. J. van der Zant, S. Michaelis de Vasconcellos, and R. Bratschkitsch, Single-photon emission from localized excitons in an atomically thin semiconductor, *Optica* **2**, 347 (2015).
- [2] A. Srivastava, M. Sidler, A. V. Allain, D. S. Lembke, A. Kis, and A. Imamoglu, Optically active quantum dots in monolayer WSe<sub>2</sub>, *Nat. Nanotechnol.* **10**, 491 (2015).
- [3] M. Koperski, K. Nogajewski, A. Arora, V. Cherkov, P. Mallet, J.-Y. Veuillen, J. Marcus, P. Kossacki, and M. Potemski, Single photon emitters in exfoliated WSe<sub>2</sub> structures, *Nat. Nanotechnol.* **10**, 503 (2015).
- [4] Y.-M. He, G. Clark, J. R. Schaibley, Y. He, M.-C. Chen, Y.-J. Wei, X. Ding, Q. Zhang, W. Yao, X. Xu, C.-Y. Lu, and J.-W. Pan, Single quantum emitters in monolayer semiconductors, *Nat. Nanotechnol.* **10**, 497 (2015).
- [5] C. Chakraborty, L. Kinnischtzke, K. M. Goodfellow, R. Beams, and a. N. Vamivakas, Voltage-controlled quantum light from an atomically thin semiconductor, *Nat. Nanotechnol.* **10**, 507 (2015).
- [6] A. Branny, S. Kumar, R. Proux, and B. D. Gerardot, Deterministic strain-induced arrays of quantum emitters in a two-dimensional semiconductor, *Nat. Commun.* **8**, 15053 (2017).
- [7] C. Palacios-Berraquero, D. M. Kara, A. R.-P. Montblanch, M. Barbone, P. Latawiec, D. Yoon, A. K. Ott, M. Loncar, A. C. Ferrari, and M. Atatüre, Large-scale quantum-emitter arrays in atomically thin semiconductors, *Nat. Commun.* **8**, 15093 (2017).
- [8] J. Cambiasso, G. Grinblat, Y. Li, A. Rakovich, E. Cortés, and S. A. Maier, Bridging the Gap between Dielectric Nanophotonics and the Visible Regime with Effectively Lossless Gallium Phosphide Antennas, *Nano Lett.* **17**, 1219 (2017).
- [9] L. Sortino, P. G. Zotev, S. Mignuzzi, J. Cambiasso, D. Schmidt, A. Genco, M. Aßmann, M. Bayer, S. A. Maier, R. Sapienza, and A. I. Tartakovskii, Enhanced light-matter interaction in an atomically thin semiconductor coupled with dielectric nano-antennas, *Nat. Commun.* **10**, 5119 (2019).
- [10] L. Sortino, M. Brooks, P. G. Zotev, A. Genco, J. Cambiasso, S. Mignuzzi, S. A. Maier, G. Burkard, R. Sapienza, and A. I. Tartakovskii, Dielectric Nanoantennas for Strain Engineering in Atomically Thin Two-Dimensional Semiconductors, *ACS Photonics* **7**, 2413 (2020).
- [11] G. Wang, A. Chernikov, M. M. Glazov, T. F. Heinz, X. Marie, T. Amand, and B. Urbaszek, Colloquium :

- Excitons in atomically thin transition metal dichalcogenides, *Rev. Mod. Phys.* **90**, 021001 (2018).
- [12] J. Lindlau, M. Selig, A. Neumann, L. Colombier, J. Förste, V. Funk, M. Förg, J. Kim, G. Berghäuser, T. Taniguchi, K. Watanabe, F. Wang, E. Malic, and A. Högele, The role of momentum-dark excitons in the elementary optical response of bilayer WSe<sub>2</sub>, *Nat. Commun.* **9**, 2586 (2018).
  - [13] M. Feierabend, S. Brem, and E. Malic, Optical fingerprint of bright and dark localized excitonic states in atomically thin 2D materials, *Phys. Chem. Chem. Phys.* **21**, 26077 (2019).
  - [14] L. Linhart, M. Paur, V. Smejkal, J. Burgdörfer, T. Mueller, and F. Libisch, Localized Intervalley Defect Excitons as Single-Photon Emitters in WSe<sub>2</sub>, *Phys. Rev. Lett.* **123**, 146401 (2019).
  - [15] C. K. Dass, M. A. Khan, G. Clark, J. A. Simon, R. Gibson, S. Mou, X. Xu, M. N. Leuenberger, and J. R. Hendrickson, Ultra-Long Lifetimes of Single Quantum Emitters in Monolayer WSe<sub>2</sub>/hBN Heterostructures, *Adv. Quantum Technol.* **2**, 1900022 (2019).
  - [16] C. Palacios-Berraquero, M. Barbone, D. M. Kara, X. Chen, I. Goykhman, D. Yoon, A. K. Ott, J. Beiter, K. Watanabe, T. Taniguchi, A. C. Ferrari, and M. Atatüre, Atomically thin quantum light-emitting diodes, *Nat. Commun.* **7**, 12978 (2016).
  - [17] S. Schwarz, A. Kozikov, F. Withers, J. K. Maguire, A. P. Foster, S. Dufferwiel, L. Hague, M. N. Makhonin, L. R. Wilson, A. K. Geim, K. S. Novoselov, and A. I. Tartakovskii, Electrically pumped single-defect light emitters in WSe<sub>2</sub>, *2D Mater.* **3**, 025038 (2016).
  - [18] G. Clark, J. R. Schaibley, J. Ross, T. Taniguchi, K. Watanabe, J. R. Hendrickson, S. Mou, W. Yao, and X. Xu, Single Defect Light-Emitting Diode in a van der Waals Heterostructure, *Nano Lett.* **16**, 3944 (2016).
  - [19] M. Blauth, M. Jürgensen, G. Vest, O. Hartwig, M. Precht, J. Cerne, J. J. Finley, and M. Kaniber, Coupling Single Photons from Discrete Quantum Emitters in WSe<sub>2</sub> to Lithographically Defined Plasmonic Slot Waveguides, *Nano Lett.* **18**, 6812 (2018).
  - [20] F. Peyskens, C. Chakraborty, M. Muneeb, D. Van Thourhout, and D. Englund, Integration of single photon emitters in 2D layered materials with a silicon nitride photonic chip, *Nat. Commun.* **10**, 4435 (2019).
  - [21] L. C. Flatten, L. Weng, A. Branny, S. Johnson, P. R. Dolan, A. A. P. Trichet, B. D. Gerardot, and J. M. Smith, Microcavity enhanced single photon emission from two-dimensional WSe<sub>2</sub>, *Appl. Phys. Lett.* **112**, 191105 (2018).
  - [22] Y.-M. He, O. Iff, N. Lundt, V. Baumann, M. Davanco, K. Srinivasan, S. Höfling, and C. Schneider, Cascaded emission of single photons from the biexciton in monolayered WSe<sub>2</sub>, *Nat. Commun.* **7**, 13409 (2016).
  - [23] X. Lu, X. Chen, S. Dubey, Q. Yao, W. Li, X. Wang, Q. Xiong, and A. Srivastava, Optical initialization of a single spin-valley in charged WSe<sub>2</sub> quantum dots, *Nat. Nanotechnol.* **14**, 426 (2019).
  - [24] Y. Luo, G. D. Shepard, J. V. Ardelean, D. A. Rhodes, B. Kim, K. Barmak, J. C. Hone, and S. Strauf, Deterministic coupling of site-controlled quantum emitters in monolayer WSe<sub>2</sub> to plasmonic nanocavities, *Nat. Nanotechnol.* **13**, 1137 (2018).
  - [25] M. Caldarola, P. Albella, E. Cortés, M. Rahmani, T. Roschuk, G. Grinblat, R. F. Oulton, A. V. Bragas, and S. A. Maier, Non-plasmonic nanoantennas for surface enhanced spectroscopies with ultra-low heat conversion, *Nat. Commun.* **6**, 7915 (2015).
  - [26] K. Koshelev and Y. Kivshar, Dielectric Resonant Metaphotonics, *ACS Photonics* **8**, 102 (2021).
  - [27] P. Kolchin, N. Pholchai, M. H. Mikkelsen, J. Oh, S. Ota, M. S. Islam, X. Yin, and X. Zhang, High Purcell Factor Due To Coupling of a Single Emitter to a Dielectric Slot Waveguide, *Nano Lett.* **15**, 464 (2015).
  - [28] A. F. Cihan, A. G. Curto, S. Raza, P. G. Kik, and M. L. Brongersma, Silicon Mie resonators for highly directional light emission from monolayer MoS<sub>2</sub>, *Nat. Photonics* **12**, 284 (2018).
  - [29] A. F. Koenderink, Single-Photon Nanoantennas, *ACS Photonics* **4**, 710 (2017).
  - [30] P. Albella, M. A. Poyli, M. K. Schmidt, S. A. Maier, F. Moreno, J. J. Sáenz, and J. Aizpurua, Low-Loss Electric and Magnetic Field-Enhanced Spectroscopy with Subwavelength Silicon Dimers, *J. Phys. Chem. C* **117**, 13573 (2013).
  - [31] S. Mignuzzi, S. Vezzoli, S. A. R. Horsley, W. L. Barnes, S. A. Maier, and R. Sapienza, Nanoscale Design of the Local Density of Optical States, *Nano Lett.* **19**, 1613 (2019).
  - [32] R. Brouri, A. Beveratos, J.-P. Poizat, and P. Grangier, Photon antibunching in the fluorescence of individual color centers in diamond, *Opt. Lett.* **25**, 1294 (2000).
  - [33] S. Morozov, E. L. Pensa, A. H. Khan, A. Polovitsyn, E. Cortés, S. A. Maier, S. Vezzoli, I. Moreels, and R. Sapienza, Electrical control of single-photon emission in highly charged individual colloidal quantum dots, *Sci. Adv.* **6**, eabb1821 (2020).
  - [34] X. Liu and M. C. Hersam, 2D materials for quantum information science, *Nat. Rev. Mater.* **4**, 669 (2019).
  - [35] R. J. Warburton, C. Schäfflein, D. Haft, F. Bickel, A. Lorke, K. Karrai, J. M. Garcia, W. Schoenfeld, and P. M. Petroff, Optical emission from a charge-tunable quantum ring, *Nature* **405**, 926 (2000).
  - [36] C.-H. Chang, X. Fan, S.-H. Lin, and J.-L. Kuo, Orbital analysis of electronic structure and phonon dispersion in MoS<sub>2</sub>, MoSe<sub>2</sub>, WS<sub>2</sub> and WSe<sub>2</sub> monolayers under strain, *Phys. Rev. B* **88**, 195420 (2013).
  - [37] T. Godde, D. Schmidt, J. Schmutzler, M. Aßmann, J. Debus, F. Withers, E. M. Alexeev, O. Del Pozo-Zamudio, O. V. Skrypkina, K. S. Novoselov, M. Bayer, and A. I. Tartakovskii, Exciton and trion dynamics in atomically thin MoSe<sub>2</sub> and WSe<sub>2</sub> : Effect of localization, *Phys. Rev. B* **94**, 165301 (2016).
  - [38] H. H. Fang, B. Han, C. Robert, M. A. Semina, D. Lagarde, E. Courtade, T. Taniguchi, K. Watanabe, T. Amand, B. Urbaszek, M. M. Glazov, and X. Marie, Control of the Exciton Radiative Lifetime in van der Waals Heterostructures, *Phys. Rev. Lett.* **123**, 067401 (2019).
  - [39] S. Mouri, Y. Miyauchi, M. Toh, W. Zhao, G. Eda, and K. Matsuda, Nonlinear photoluminescence in atomically thin layered WSe<sub>2</sub> arising from diffusion-assisted exciton-exciton annihilation, *Phys. Rev. B* **90**, 155449 (2014).
  - [40] M. Danovich, V. Zolyomi, V. I. Fal'ko, and I. L. Aleiner, Auger recombination of dark excitons in WS<sub>2</sub> and WSe<sub>2</sub> monolayers, *2D Mater.* **3**, 035011 (2016).
  - [41] A. J. Brash, J. Iles-Smith, C. L. Phillips, D. P. S. McCutcheon, J. O'Hara, E. Clarke, B. Royall, L. R. Wilson, J. Mørk, M. S. Skolnick, A. M. Fox, and A. Nazir, Light Scattering from Solid-State Quantum Emitters: Beyond the Atomic Picture, *Phys. Rev. Lett.* **123**, 167403 (2019).

- [42] P. Dey, J. Paul, Z. Wang, C. E. Stevens, C. Liu, A. H. Romero, J. Shan, D. J. Hilton, and D. Karauskaj, Optical Coherence in Atomic-Monolayer Transition-Metal Dichalcogenides Limited by Electron-Phonon Interactions, *Phys. Rev. Lett.* **116**, 127402 (2016).
- [43] J. Klein, L. Sigl, S. Gyger, K. Barthelmi, M. Florian, S. Rey, T. Taniguchi, K. Watanabe, F. Jahnke, C. Kastl, V. Zwiller, K. D. Jöns, K. Müller, U. Wurstbauer, J. J. Finley, and A. W. Holleitner, Engineering the Luminescence and Generation of Individual Defect Emitters in Atomically Thin MoS<sub>2</sub>, *ACS Photonics* **8**, 669 (2021).
- [44] E. M. Alexeev, A. Catanzaro, O. V. Skrypka, P. K. Nayak, S. Ahn, S. Pak, J. Lee, J. I. Sohn, K. S. Novoselov, H. S. Shin, and A. I. Tartakovskii, Imaging of Inter-layer Coupling in van der Waals Heterostructures Using a Bright-Field Optical Microscope, *Nano Lett.* **17**, 5342 (2017).
- [45] A. Castellanos-Gomez, M. Buscema, R. Molenaar, V. Singh, L. Janssen, H. S. J. van der Zant, and G. A. Steele, Deterministic transfer of two-dimensional materials by all-dry viscoelastic stamping, *2D Mater.* **1**, 011002 (2014).

**Acknowledgments** L. S., P. G. Z. and A. I. T. thank the financial support of the European Graphene Flagship Project under grant agreements 881603 and EPSRC grant EP/S030751/1. L. S. and A. I. T. thank the European Union’s Horizon 2020 research and innovation programme under ITN Spin-NANO Marie Skłodowska-Curie grant agreement no. 676108. P. G. Z. and A.

I. T. thank the European Union’s Horizon 2020 research and innovation programme under ITN 4PHOTON Marie Skłodowska-Curie grant agreement no. 721394. J. C., S. A. M., and R. S. acknowledge funding by EPSRC (EP/P033369 and EP/M013812). C. L. P., A. J. B., A. I. T. and A. M. F. acknowledge funding by EPSRC Programme Grant EP/N031776/1. S. A. M. acknowledges the Lee-Lucas Chair in Physics, the Solar Energies go Hybrid (SolTech) programme, and the Deutsche Forschungsgemeinschaft (DFG, German Research Foundation) under Germany’s Excellence Strategy – EXC 2089/1 – 390776260.

**Author contributions** L. S., P. G. Z., A. I. T., S. A. M. and R. S. conceived the idea of the experiment. L. S. and P. G. Z. fabricated WSe<sub>2</sub> layers, transferred them on GaP nano-antennas, and carried out numerical modelling. L. S., P. G. Z., C. L. P. and A. J. B. carried out optical spectroscopy measurements on WSe<sub>2</sub>. J. C. fabricated GaP nano-antennas. J. C. and R. S. designed GaP nano-antennas. L. S. and E. M. conceived and solved the rate equation model. L. S., P. G. Z., C. L. P., A. J. B. and A. I. T. analysed optical spectroscopy data. S. A. M., R. S., A. M. F. and A. I. T. managed various aspects of the project. L. S., P. G. Z. and A. I. T. wrote the manuscript with contributions from all co-authors. A. I. T. oversaw the whole project.



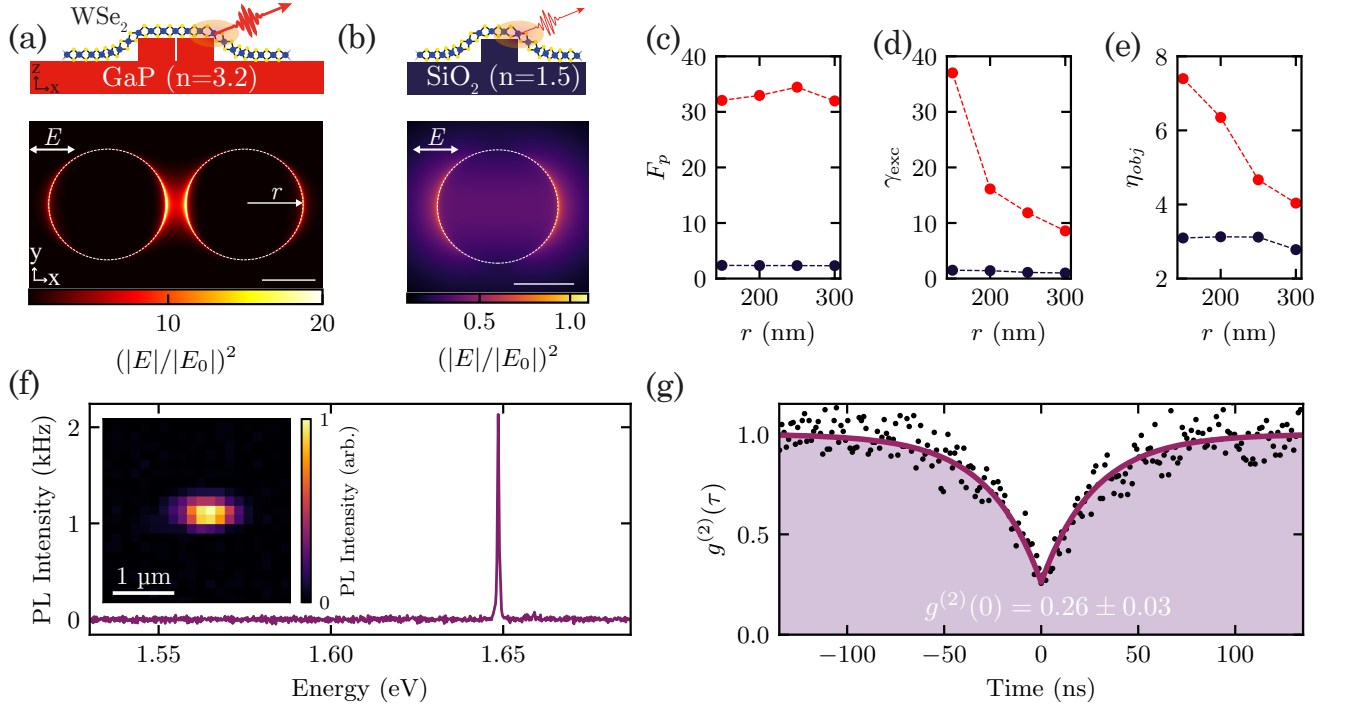


**FIG. 1. Optical properties of nano-antennas and single-photon emitters in monolayer WSe<sub>2</sub>.** (a, b) Top panel: schematics of monolayer WSe<sub>2</sub> on top of GaP nano-antennas (a) and SiO<sub>2</sub> nano-pillar (b). Lower panel: calculated relative intensity of the electric field in the scattered wave ( $E$ ) over that in the incident wave ( $E_0$ ). Results are shown for (a) a GaP dimer nano-antenna ( $r = 150$  nm,  $h = 200$  nm,  $gap = 50$  nm) and (b) SiO<sub>2</sub> nano-pillar ( $r = 150$  nm,  $h = 100$  nm). The calculated intensity is shown for the plane at the top of each structure. Scale bar: 150 nm. (c-e) The calculated Purcell enhancement factor (c), excitation rate (d) and light collection efficiency (e) for a dipole emitter placed at the position of the highest field enhancement shown in (a) and (b) of the GaP dimer nano-antennas (red) and SiO<sub>2</sub> nano-pillars (blue) relative to the same parameters for this dipole in vacuum. See further details in Methods and Supplementary Note II. (f) A  $T = 4$  K PL spectrum of a WSe<sub>2</sub> SPE on a GaP nano-antenna ( $r = 250$  nm,  $h = 200$  nm,  $gap = 50$  nm), excited with a 638 nm pulsed laser with 20 MHz repetition rate and an average power of 15 nW. Inset: Map of the integrated PL intensity of this monolayer ( $T = 4$  K). (g) Second order photon correlation curve for the PL signal in (f).

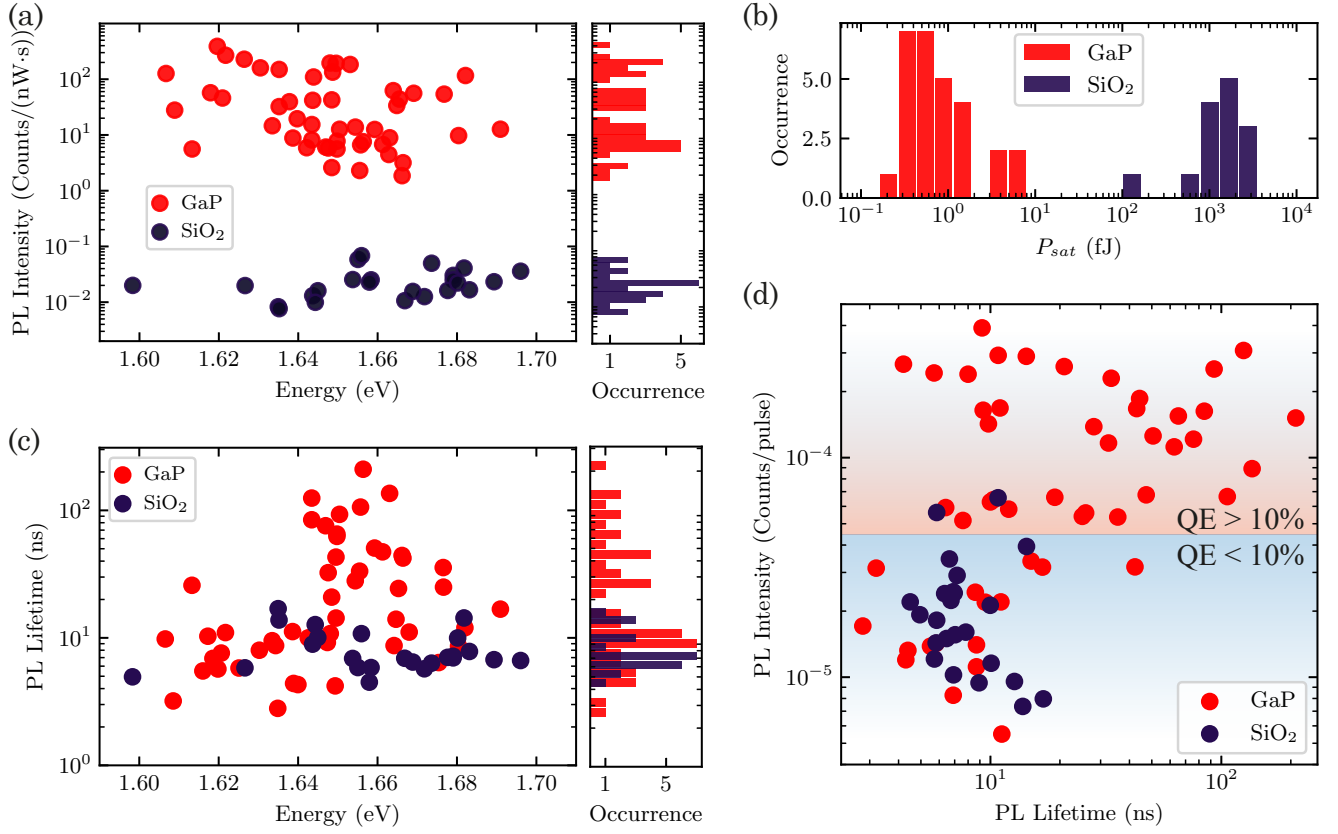
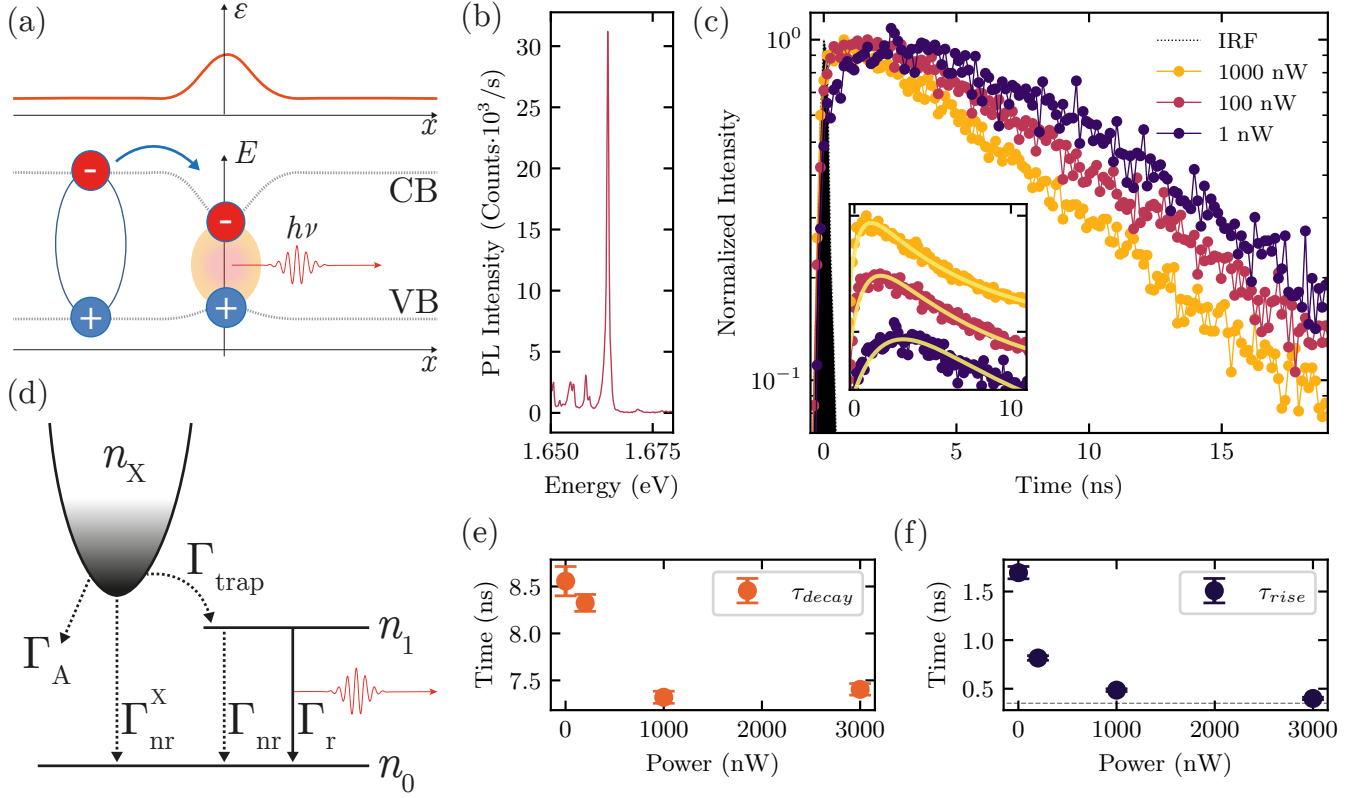


FIG. 2. **Comparison of optical properties of SPEs formed on GaP dimer nano-antennas and on SiO<sub>2</sub> nano-pillars.** Data for SPEs on GaP dimer nano-antennas is shown in red and for SPEs on SiO<sub>2</sub> nano-pillars is shown in blue. (a) PL intensity normalized by the average laser excitation power measured in the SPE saturation regime. The histogram on the right shows the occurrence of the observed PL intensity values. (b) Energy per laser pulse required for SPE saturation,  $P_{sat}$ . See Supplementary Fig.4 for more details on how  $P_{sat}$  is extracted from the PL data. (c) PL decay times (main plot) and its occurrence (right). (d) SPE PL peak intensity divided by the laser repetition rate plotted versus SPE PL decay time. The red and blue areas of the plot correspond to SPEs with QE > 10% and QE < 10%, respectively. See main text and Supplementary Note VI for more details of how QE was estimated.



**FIG. 3. PL dynamics in SPEs coupled to GaP nano-antennas.** (a) Schematic showing the conduction (CB) and valence band (VB) behavior as a function of strain (shown in the top panel with a red line), and a single exciton trapping from the reservoir in 2D WSe<sub>2</sub> into a strain-induced potential minimum, giving rise to the non-classical light red-shifted from the emission in the unstrained monolayer. (b) Time-integrated PL spectrum of the strain-induced WSe<sub>2</sub> SPE with a QE of 86% and saturation power of 57 nW for 80 MHz repetition rate, for which the data in (c), (e) and (f) are presented. (c) PL decay curves for the SPE in (b) measured at different laser powers. The instrument response function (IRF) is shown in grey. Inset: zoom-in of the PL traces also showing fitting with the analytical model discussed in Supplementary Note VII. The PL traces in the inset are plotted on a linear scale and shifted vertically for display purposes. (d) Schematic of the three level system representing the dark exciton reservoir ( $n_X$ ), the exciton in the SPE ( $n_1$ ) and the ground level ( $n_0$ ), and the processes describing radiative and non-radiative decay of  $n_X$  and  $n_1$  populations. See text for more details. (e,f) PL decay (e) and PL rise (f) times, as a function of the excitation power, obtained from the data fitting in Fig.3c. For 3000 nW,  $\tau_{rise}$  approaches the instrument resolution (grey dashed line).

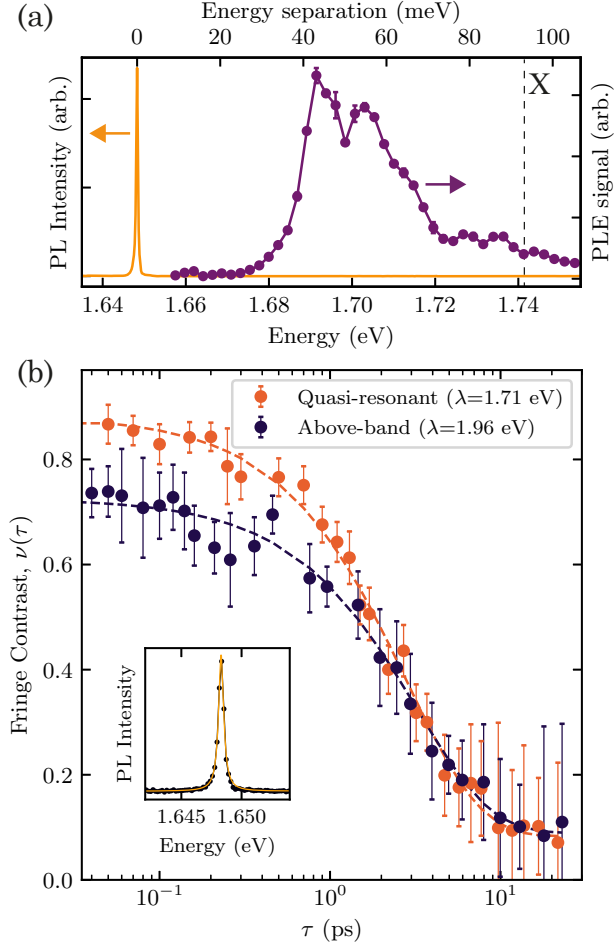


FIG. 4. **Measurements of SPE coherence.** (a) PL emission (yellow) and the PL excitation (PLE) spectra (purple) from a WSe<sub>2</sub> SPE. The PLE signal exhibits a series of confined exciton peaks below the neutral exciton PL peak position (X). (b) Interference fringe contrast,  $\nu(\tau)$  for two different excitation laser wavelengths. The above band excitation (blue dots) is obtained at 1.96 eV (638 nm) and yields a coherence time of  $T_2 = 2.83 \pm 0.20$  (fitting shown with a dashed line). The quasi-resonant excitation (orange dots) is obtained with a laser tuned to 1.71 eV (725 nm), lower than the A-exciton in unstrained monolayer WSe<sub>2</sub>, yielding a coherence time of  $T_2 = 3.12 \pm 0.40$ . Inset: SPE PL spectrum under the quasi-resonant excitation (black dots) fitted with a single Lorentzian peak (yellow solid line) with a linewidth of  $450 \mu\text{eV}$ , corresponding to a coherence time of  $T_2 = 2.9$  ps, in close agreement with the values obtained from the interferometric measurements.